MATERIALS CHEMISTRY FRONTIERS

RESEARCH ARTICLE

View Article Online
View Journal

Cite this: DOI: 10.1039/d5qm00667h

3D printed water-stable Cd-doped $Cs_4MnBi_2Cl_{12}$/polylactic acid perovskite/polymer composites for high-flux X-ray scintillation

Amr Elattar, *[a] Abdullah Al Noman,[a] Akil Dyson,[a] J. S. Raaj Vellore Winfred,[b] Burak Guzelturk,[c] Logan T. Kearney,[d] Adrienn Maria Szucs[e] and Tarik Dickens*[a]

Stable and efficient X-ray scintillators are crucial for medical diagnostics, industrial, and defense applications. However, conventional scintillator technologies face a trade-off between stability, optimal performance, and sustainability. Herein, we introduce 3D-printed $Cs_4MnBi_2Cl_{12}$ (Pero1) and $Cs_4Cd_{0.68}Mn_{0.32}Bi_2Cl_{12}$ (Pero2) perovskite microcrystals embedded within a polylactic acid (PLA) polymer composite as X-ray scintillators, combining efficiency, stability, and sustainability. The orange luminescent perovskite powder phosphors exhibited poor water stability, which was successfully addressed through incorporation into PLA *via* filament extrusion and fused deposition modeling (FDM) 3D printing. The resulting composite films demonstrated remarkable water stability while maintaining uniform orange emission throughout the polymer matrix, as confirmed by 3D topography scanning and X-ray fluorescence mapping. Structural characterization revealed minimal chemical interaction between the perovskite and PLA matrix, with the composites retaining their crystalline properties. The PLA-Pero2 composite exhibited superior optical properties, with a photoluminescence quantum yield of 47%, nearly 17 times higher than that of PLA-Pero1 (2.8%), attributed to the effective suppression of non-radiative decay pathways through Cd^{2+} doping. Under hard X-ray irradiation at synchrotron beamlines, both composites exhibited excellent radioluminescence, with emission peaks at 605 nm, a linear response across a wide X-ray flux range, and remarkable radiation stability, showing less than 3% intensity degradation after 600 seconds of continuous high-dose exposure. The PLA-Pero2 composite achieved a spatial resolution of 5 line pairs per millimeter and a contrast ratio of 0.255. These performance metrics, combined with the polymer's biodegradability and scalability through additive manufacturing, position PLA-based composites as a more sustainable alternative to conventional petroleum-based polymer scintillators for next-generation medical imaging, radiation monitoring, and industrial radiography applications.

Received 7th September 2025,
Accepted 5th January 2026

DOI: 10.1039/d5qm00667h

rsc.li/frontiers-materials

1. Introduction

Halide perovskites (HPs) have emerged as groundbreaking materials across diverse applications, including solar cells,[1,2] photodetectors,[3–5] light-emitting diodes,[6,7] and X-ray scintillators[8–10] due to their exceptional optoelectronic properties such as high absorption coefficients, bandgap tunability, superior charge carrier mobility, and excellent photoluminescence quantum yields.[11–15] Despite the significant features of HP materials as X-ray scintillators including high light yields, fast decay times, and efficient radioluminescence conversion, making them highly attractive for medical imaging and radiation detection systems,[16,17] the practical implementation of pristine halide perovskites is hindered by several challenges including moisture sensitivity,[18–20] thermal instability,[21,22] processing difficulties,[23,24] and poor mechanical stability[25,26] that limit their direct application in real-world scintillation devices. Consequently, there is an ongoing search to address these limitations through developing perovskite/polymer composites scintillators that combine all essential attributes of an effective scintillator: improved spatial resolution and processability.[16] Several polymers have been developed for use in perovskite composite-based X-ray scintillators, including polymethyl methacrylate (PMMA),[27–29] polystyrene (PS),[30–32] polybutyl

[a] *Industrial & Manufacturing Engineering, FAMU-FSU College of Engineering, 2525 Pottsdamer St., Tallahassee, Florida 32310, USA. E-mail: ae23e@fsu.edu, dickens@eng.famu.fsu.edu*
[b] *Department of Chemistry and Biochemistry, Florida State University, Tallahassee, FL, 32306, USA*
[c] *X-ray Science Division, Argonne National Laboratory, Lemont, IL, USA*
[d] *Carbon and Composites Group, Chemical Sciences Division, Oak Ridge National Laboratory, Oak Ridge, TN, 37830, USA*
[e] *Center for Rare Earths, Critical Minerals, and Industrial Byproducts, National High Magnetic Field Laboratory, Florida State University, USA*

methacrylate (PBMA),[33] polyvinylidene fluoride (PVDF),[34,35] and polydimethylsiloxane (PDMS).[36,37] While these polymers offer advantages such as good thermal stability, flexibility, and high optical transparency, they are not considered environmentally sustainable. This is primarily due to their non-biodegradability—petroleum-based polymers (PMMA, PS, and PBMA), silicon-based polymers (PDMS), and fluorine-based polymers (PVDF) are extremely persistent in the environment and challenging to recycle. Compared to these polymers, polylactic acid (PLA), a thermoplastic aliphatic polyester derived from renewable resources, demonstrates superior environmental sustainability, biocompatibility, and processability while maintaining excellent chemical stability necessary for practical scintillation applications.[38,39] The integration of PLA with HPs materials has gained considerable attention in recent literature. Tabbassum *et al.* developed a highly stable $FAPbBr_3$/PLA nanofibrous membrane using the electrospinning method.[40] Moreover, a 3D-printed $CsPbBr_3$/PLA film, with a thickness of 600 μm, has demonstrated a promising candidate for X-ray scintillation.[41]

Lead-free $Cs_4MnBi_2Cl_{12}$ double perovskite, with structure $A_4MM'X_{12}$ where Cs occupies the A-site, Mn^{2+} and Bi^{3+} occupy the metal sites, and Cl serves as the halide, exhibits excellent chemical stability compared to conventional lead-based perovskites.[42] Owing to the effective energy transfer from $[BiCl_6]^{3-}$ octahedron donor to $[MnCl_6]^{4-}$ acceptor, $Cs_4MnBi_2Cl_{12}$ was shown to be a phosphor with an efficient orange emission at 610 nm, with photoluminescence quantum yield (PLQY) of up to 25.7%, making it a good candidate as a soft X-ray scintillator.[43] The incorporation of Mn^{2+} ions introduces d–d transitions that contribute to the material's scintillation properties, while the Bi^{3+} ions provide heavy atom effects beneficial for X-ray absorption, making $Cs_4MnBi_2Cl_{12}$ an attractive candidate for radiation detection applications with reduced toxicity concerns compared to lead-based alternatives. It has been recognized that the introduction of lanthanides (La^{3+}) and indium (In^{3+}) as dopants into $Cs_4MnBi_2Cl_{12}$ can effectively tune its optoelectronic properties.[44,45] Moreover, Cd^{2+}-doped $Cs_4MnBi_2Cl_{12}$ was reported to enhance the PLQY to 57%.[46]

In this work, we present a thorough investigation of a 3D printed Cd-doped $Cs_4MnBi_2Cl_{12}$/PLA composite film for X-ray scintillation applications, combining the structural stability of the lead-free double perovskite with the exceptional processability and biocompatibility of PLA polymer matrix. We demonstrated the successful incorporation of perovskite microcrystals into PLA filament and their suitability for the fused deposition modeling (FDM) 3D printing process. We characterize the structural, thermal, and optical properties, as well as the long-term stability of the 3D printed composite film under water exposure. Additionally, we evaluate its X-ray scintillation performance, including imaging, linearity measurements, and spatial resolution assessment under X-ray irradiation. This research aims to establish a new paradigm for sustainable, durable, and efficient X-ray scintillation devices through the integration of lead-free perovskites with additive manufacturing technologies.

2. Experimental

2.1. Chemicals

Cesium chloride CsCl (≥99%), Cadmium oxide CdO (≥99%), manganese(II) oxide MnO (≥99%), bismuth(III) oxide Bi_2O_3 (≥99%), as raw materials were purchased from Sigma-Aldrich. Polylactic acid PLA granules were purchased from 3Devo. Hydrochloric acid (HCl, 37%) was used as the solvent for the perovskite microcrystals preparation. Isopropyl alcohol (IPA) was used for washing the perovskite microcrystals. All reagents and solvents were used without further purification.

2.2. Synthesis of perovskite microcrystals

The preparation of Pero1 and Pero2 followed the literature procedure with some modification.[46] To prepare Pero1, 1 mmol of MnO and 1 mmol of Bi_2O_3 were dissolved in 4 mL of HCl at room temperature, while stirring magnetically. For Pero2, 0.32 mmol of MnO, 0.68 mmol of CdO, and 1 mmol of Bi_2O_3 were dissolved in the same 4 mL of HCl. After these initial solutions were prepared, 4 mmol of CsCl, dissolved in 1 mL of HCl, was added, resulting in the formation of perovskite precipitates. The precipitates were then washed with isopropyl alcohol (IPA), leading to the formation of Pero1/Pero2 microcrystals. The final samples were dried at 70 °C.

2.3. Preparation of PLA-Pero composite filament

PLA granules were mixed with 5 wt% perovskite powder to prepare the composite filaments. The mixture was processed using the 3Devo Filament Maker, a high-precision filament production system designed for small-scale material development, with a 1.75 mm diameter. The equipment enabled precise temperature and extrusion control, ensuring the uniform dispersion of perovskite particles within the PLA matrix. This step is critical to achieving consistent mechanical and functional properties in the final filament.

2.4. Preparation of 3D printed PLA-Pero composite

The resulting composite filaments were subsequently used to fabricate 3D printed PLA-Pero composites using fused deposition modelling (FDM) 3D printer (nscrypt-300). The bone structure shown in Fig. 1e serves as a proof-of-concept for complex geometries, while the flat square films in Fig. 1f were specifically designed for scintillation characterization.

2.5. Characterization

Raman measurement was performed using a Reinshaw, Inc. inVia Raman microscope in the range of 50–3500 cm^{-1}, using 785 nm edge laser. The X-ray diffraction (XRD) measurements for PLA and PLA-perovskite composite films were performed using the Rigaku SmartLab diffractometer with Cu Kα radiation operating at a voltage of 40 kV and a current of 45 mA. X-ray scattering measurements were collected on a Xeuss 3.0 (Xenocs, France) equipped with a D2+ MetalJet X-ray source (Ga Kα,

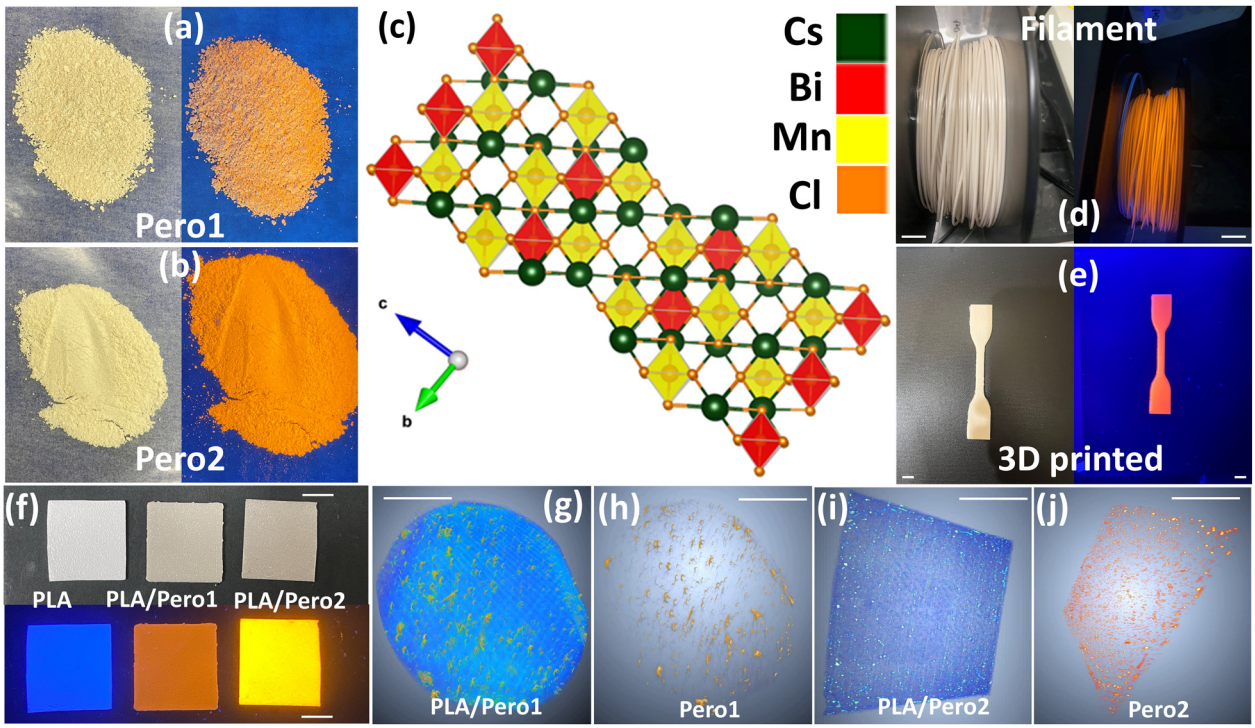

Fig. 1 $Cs_4MnBi_2Cl_{12}$ (a) and Cd-doped $Cs_4MnBi_2Cl_{12}$ (b) perovskite powders prepared *via* HCl method, under white and UV light. (c) Crystal structure of $Cs_4MnBi_2Cl_{12}$ perovskite. The PLA/perovskite composite filament (d) and 3D printed bone structure (e) are shown under white and UV light. The 3D printed thick films of PLA, PLA-Pero1, and PLA-Pero2 composites (f) are demonstrated under white and UV light. 3D Topography scan of the printed PLA/Pero1 (g) and PLA/Pero2 (i) films. Distribution of Pero1 (h) and Pero2 (j) microcrystals within the PLA matrix. "Scale bar = 1 cm".

9.2 keV, λ = 1.3414 Å). Printed polymer layers were adhered to the solids sample holder, aligned perpendicular to the direction of the incident beam (transmission mode), measured for 3 min and 20 min at sample-to-detector distances of 47 and 900 mm, respectively. All measurements were taken following calibration with a LaB_6 standard. 2D images of the scattering patterns were collected on a Eiger 2R 4 M hybrid photon counting detector with a pixel dimension of 75 × 75 μm^2 (Dectris, Switzerland). TGA and DSC thermal analysis were obtained using Universal V4.5A TA Instruments. The temperature was ramped at a rate of 10 °C min^{-1} under N_2 flow at 60 ml min^{-1}. Micro X-ray fluorescence (microXRF) data were collected using a Bruker M4 Plus Micro-XRF spectrometer, equipped with a Rh X-ray source operating at 50 kV and 600 μA. The spot size was 20 μm. 3D CT scanning was collected using Rigaku CT Lab HX. The PLQY measurements were performed using Quantaurus C11347 spectrometer. Temperature-dependent PL measurements were carried out using LP980 transient absorption spectrometer (Edinburgh instruments) with Oxford Optistat DN cryostat. TRPL measurements were performed using the same instrument, with an excitation wavelength of 350 nm and an emission wavelength of 615 nm. PLE spectra were acquired using a Horiba Fluoromax 4 with an emission wavelength of 615 nm. Water immersion stability testing was conducted at room temperature for 24 hours in deionized water. The samples were completely submerged, and their structural and optical properties were evaluated before and after water immersion.

2.6. Radioluminescence measurements

Radioluminescence measurements were performed at the Beamline 7-ID-B of the Advanced Photon Source. Measurements were collected when APS was operating in a 216 bunch mode with 200 mA total ring current. To monochromatize the X-ray beam, (111) silicon pair monochromator was used. X-ray energy was set to 15.5 keV. X-ray flux (photons per s) impinging on the sample was calibrated using an ion chamber with a 6 cm path length located just before the sample. The size of the X-ray beam on the sample was measured using an X-ray eye with a calibrated CCD camera. The beam size was 700 μm (horizontal) by 900 μm (vertical). X-rays arrived the sample surface through surface normal. The RL spectra were collected on the front face of the samples with a multimode fiber (core size: 1.5 mm) with a collimating lens adapter. The end of the fiber was fed into an Andor Shamrock spectrometer with a grating of 150 lines per mm and Blaze wavelength of 500 nm. The spectrometer had a Peltier cooled Andor CCD camera for detection. Input slit of the spectrometer was set to be 20 μm. Stability measurements were performed by collecting data at finite time interval with Andor Solis software under fixed X-ray flux. For linearity measurements, X-ray flux was controlled by a combination of four different thickness Mo filters to attenuate the X-ray flux at

varying steps. For the imaging experiment, Mitutoyo 1× objective and FLIR Blackfly S camera were used to image the scintillator samples when a resolution test pattern was inserted between the scintillator screen and the X-ray source. We used a test pattern (Type-39) obtained from Supertech X-ray.

3. Results and discussion

3.1. Synthesis of 3D printed perovskites/PLA films and their underwater stability

As discussed previously,[43,46] the perovskite powder $Cs_4MnBi_2Cl_{12}$ (Pero1) was synthesized using the hydrochloric acid (HCl) method, utilizing starting materials of MnO and Bi_2O_3 which were dissolved in HCl. To this solution, a pre-dissolved CsCl in HCl was added, resulting in the precipitation of a white perovskite powder denoted as Pero1. Similarly, the perovskite powder $Cs_4Cd_{0.68}Mn_{0.32}Bi_2Cl_{12}$ (Labeled as Pero2) was prepared using the same procedure, with the inclusion of $CdCl_2$ among the starting materials. Following centrifugation and washing with isopropyl alcohol (IPA), the perovskite powders were dried at 70 °C. Under white light, the perovskite powders exhibit a white color, while under UV light, Pero2 displays more intense orange emission than Pero1, as shown in Fig. 1a and b. According to the literature,[42–47] both perovskites possess rhombohedral crystal structures characterized by alternating octahedra of $[BiCl_6]^{3-}$ and $[MnCl_6]^{4-}$, as depicted in Fig. 1c. Both perovskite powder samples exhibited poor stability when exposed to water. When subjected to water, the orange emission of the perovskite powder diminished, as illustrated in Fig. 2a and b. Consequently, pristine perovskite is unsuitable for future applications in harsh environments. To address this issue, additive manufacturing was employed to enhance the stability of perovskite for greater validation and applicability under challenging conditions. Specifically, 5 wt% of perovskite powder was blended with polylactic acid (PLA) polymer granules using the 3Devo filament maker, without the addition of any solvent. The result was a highly flexible, white filament with a diameter of 1.75 mm (Fig. 1d). It is important to note that increasing the perovskite content beyond 5 wt% led to the formation of rigid, brittle filaments that exhibited poor extrudability and compromised the 3D printing process due to inadequate flexibility for proper material flow through the printer nozzle. Under UV light, this filament displayed an orange emission evenly across its surface, confirming the homogenous distribution of perovskite microcrystals embedded within the PLA matrix. Following the production of the filaments, they were utilized through nscrypt for 3D printing various shapes. As illustrated in Fig. 1e, the 3D printed dog bone structure emits a uniform orange glow under UV light. Additionally, to investigate the scintillation properties of the PLA-perovskites, we prepared 3D-printed films, as demonstrated in the supplemental video V1. The printed PLA films initially appear white; however, they exhibit noticeable darkening with the incorporation of perovskite microcrystals, as shown in Fig. 1f. Under 365 nm ultraviolet (UV) light, the emission characteristics of the films differ significantly. The

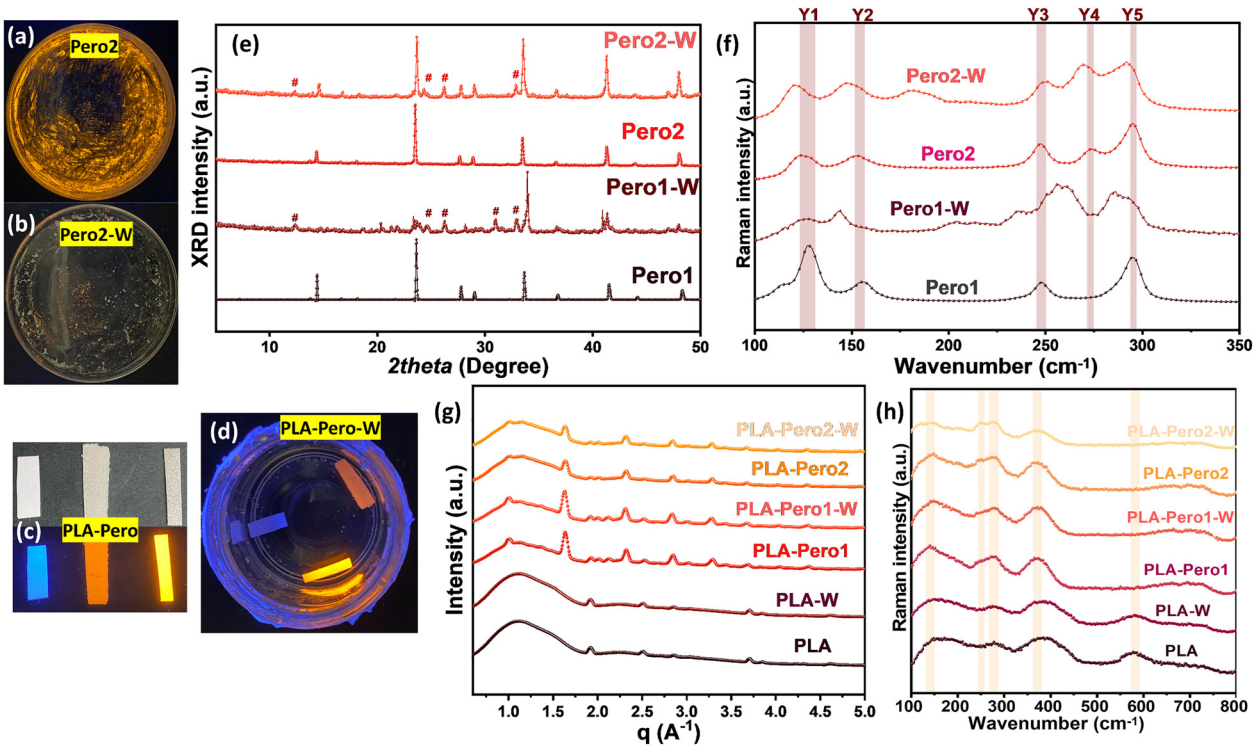

Fig. 2 Structural and vibrational characterization of perovskite powders and PLA composite films before and after water immersion stability testing. Digital photographs of perovskite powders and PLA-perovskite composites before (a) and (c) and after (b) and (d) water immersion treatment, respectively. X-ray diffraction (XRD) patterns (e) and Raman spectra (f) of perovskite powders before and after water immersion. 1D Wide-angle X-ray scattering (WAXS) patterns (g) and Raman spectra (h) of PLA and PLA-perovskite composite films before and after water immersion.

PLA film emits an intense blue light, while the PLA-Pero1 and PLA-Pero2 films display orange and deep orange emissions, respectively. To explore the distribution of perovskite microcrystals within the PLA matrix, a 3D topography scan was conducted. As demonstrated in Fig. 1g–j and Videos SV2–SV3, both PLA-perovskite films revealed a uniform distribution of perovskite microcrystals within the PLA matrix, aligning with the consistent orange emission. It should be noted that the average particle size of PLA-Pero1 and PLA-Pero2 is 500 μm and 800 μm, respectively. Remarkably, the 3D-printed films have shown enhanced stability in water, maintaining their emission under UV light without any degradation, as illustrated in Fig. 2c and d and the Video SV4. Owing to the existence of the PLA matrix, the perovskite microcrystals embedded within it have retained their chemical and optical properties. X-ray fluorescence (Micro-XRF) mapping was conducted for PLA-perovskite films for qualitative identification of perovskite elements embedded within the PLA matrix, as shown in Fig. S1. Micro-XRF mapping confirms the presence of Cs, Mn, Bi, Cl, and Cd elements through the perovskite structure as demonstrated in supplemental Table S1.

3.2. Structural properties

We characterize the structural properties of the PLA/perovskite composites, including XRD, Raman, SAXS, and WAXD measurements. The X-ray diffraction patterns (Fig. 2e) reveal significant structural modulation in both perovskite powders following water immersion treatment. The pristine Pero1 and Pero2 samples exhibit well-defined diffraction patterns characteristic of their respective rhombohedral crystal structures of $Cs_4MnBi_2Cl_{12}$ (Pero1) and Cd-doped $Cs_4MnBi_2Cl_{12}$ (Pero2) materials. Owing to the smaller effective ionic radius of Mn (80 pm) compared to Cd (95 pm), the diffraction peak positions slightly shifted toward smaller angles, that is, a larger *d*-space, due to the crystal lattice expansion with an increase in the Cd content.[48] The water-treated samples (Pero1-W and Pero2-W) exhibit the emergence of additional diffraction peaks marked with ''#'' symbols, indicating the formation of distinct secondary phases resulting from hydrolytic decomposition of the perovskite structure. This water-induced degradation leads to the breakdown of the halide perovskite framework, generating decomposition products that include metal chloride hydrates and tetragonal bismuth oxychloride (BiOCl) formed through the hydrolysis of $[BiCl_6]^{3-}$ octahedral units.[49] Additionally, it is important to note that the main Raman peaks of perovskite powders (Pero1 and Pero2), typically located in the region of 100–350 cm^{-1}, as depicted in Fig. 2f and Table S2, are shifted upon immersion in water. This observation is consistent with the findings from XRD results. Modulation in the characteristic diffraction and Raman peaks provides direct evidence for the moisture-sensitive nature of the perovskite materials, revealing the specific pathways through which structural degradation occurs upon aqueous exposure. The wide-angle X-ray diffraction (WAXD) analysis (Fig. 2g) provides critical insights into the structural changes that occur upon the incorporation of perovskite crystals into the PLA matrix. The pristine PLA sample exhibits its characteristic semi-crystalline structure, with well-defined diffraction peaks observed at q = 1.9 $Å^{-1}$ and q = 2.5 $Å^{-1}$, corresponding to diffraction angles of approximately 28.0° and 36.6°, respectively.[50] These peaks are attributed to the (200)/(110) and (203) crystallographic planes of the α-form of PLA, confirming the polymer's inherent crystalline domains. Upon formation of the PLA/perovskite composites, distinct new diffraction features emerge in the composite materials, which are attributed to the perovskite crystal structure. The appearance of these perovskite characteristic peaks confirms the successful incorporation and retention of the crystalline perovskite phase within the polymer matrix. The sharpness and intensity of these peaks indicate well-formed perovskite crystals with good crystallinity. The small-angle X-ray scattering (SAXS) measurements provide complementary evidence for the successful incorporation of perovskite particles within the PLA matrix (Fig. S2). A distinct q^{-4} intensity falloff is observed in the SAXS region for both PLA-Pero1 and PLA-Pero2 composites, which is characteristic of Porod scattering behavior. The q^{-4} scattering profile indicates that the perovskite particles possess sharp, well-defined interfaces with the PLA matrix, suggesting good phase separation and well dispersion of the perovskite microcrystals throughout the matrix without significant aggregation. The water exposure WAXS studies (PLA-W, PLA-Pero1-W, and PLA-Pero2-W) reveal interesting stability characteristics where the diffraction pattern remains largely unchanged after water exposure, indicating good structural stability of both the composite morphology and the perovskite crystals. Furthermore, the 50–3500 cm^{-1} vibrational spectrum (Fig. S3) exhibits the characteristic Raman signature with well-defined peaks corresponding to the PLA fundamental vibrational modes. Key spectral features include the C–O stretching vibrations around 870 cm^{-1}, CH_3 rocking and C–C stretching modes in the 1000–1100 cm^{-1} region, C–H bending vibrations near 1450 cm^{-1}, and the prominent C═O stretching vibration at approximately 1770 cm^{-1}, which are consistent with the expected vibrational fingerprint of polylactic acid. The most striking observation in the composite spectra is the emergence of intense new peaks in the 600–800 cm^{-1} region (highlighted in the orange shaded area) for both PLA-Pero1 and PLA-Pero2 samples. These peaks are completely absent in the pristine PLA spectrum, providing definitive evidence for the successful incorporation of perovskite crystals within the polymer matrix. The low-frequency Raman region (100–400 cm^{-1}) exhibits the appearance of the characteristic perovskite vibrational modes, confirming that the inorganic crystals retain their structural integrity during the composite formation process (Fig. 2h). Moreover, the composite materials retain their Raman peaks after water treatment, which is consistent with the XRD trend.

3.3. Thermal properties

To evaluate the thermal stability of the 3D printed samples and determine how perovskite incorporation affects the thermal transition parameters of the PLA matrix, DSC and TGA measurements were carried out. Fig. 3a shows the typical DSC thermograms of PLA, PLA/perovskite composites under the treatment of extrusion and 3D printing. Glass transition

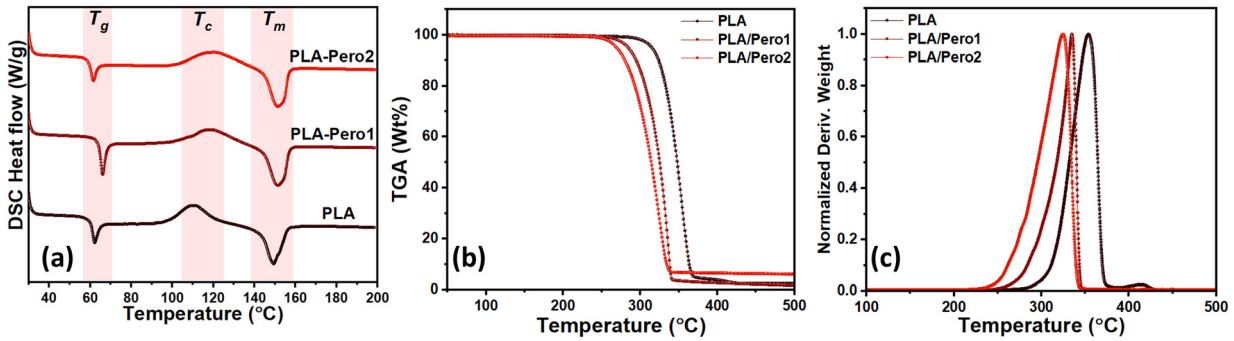

Fig. 3 Thermal characterization of PLA, PLA-Pero1, and PLA-Pero2: differential Scanning Calorimetry (DSC) (a). Thermogravimetric analysis (TGA) (b) and differential thermogravetric pattern (DTG) (c).

temperature (T_g), crystallization temperature (T_c), melting temperature (T_m), crystallization enthalpy (ΔH_c), and melting enthalpy (ΔH_m) of PLA and PLA/perovskite composites were determined from the heating cycles, as summarized in Table 1. According to the previous work,[51] the degree of crystallinity (X_c) of the PLA-based composites can be calculated from eqn (1) as follows:

$$X_c\ (\%) = \frac{\Delta H}{\Delta H_m^\circ} \times \left(1 - \frac{\text{wt\% filler}}{100}\right) \times 100 \qquad (1)$$

where the $\Delta H = \Delta H_m - \Delta H_{cc}$ in the heating cycle, and ΔH_{cc} is the cold crystallization enthalpy. ΔH_m° is the melting enthalpy of 100% crystalline polymer, which was taken to be 93.6 J g^{-1} for PLA.[52] ΔH_{cc} was replaced by ΔH_c in this research. The calculated X_c values are listed in Table 1. It is obvious that the X_c for PLA-Pero2 is the largest and that for PLA is the lowest, owing to the crystalline and amorphous structures of perovskite and PLA, respectively. These results are in accordance with the results of XRD diffraction, in which PLA-Pero2 shows obvious crystalline peaks and PLA-Pero1 presents weak crystalline peaks, whereas PLA shows mainly amorphous diffraction peaks. Additionally, the crystallization and melting temperatures of PLA/perovskite composites are clearly shifted to higher temperatures compared to pristine PLA, further indicating that the degree of crystallinity significantly increases with the addition of perovskite. The thermal stability of printed PLA/perovskite composites was studied through thermogravimetric analysis (TGA), as depicted in Fig. 3b. The perovskite crystals have demonstrated a high thermal stability with a decomposition temperature above 400 °C, as shown in Fig. S4. According to the DTG curves in Fig. 3c, all the printed samples have only one decomposition stage, suggesting that only PLA decomposed due to the existence of PLA polymer as a major content in the printed composites. The weight loss shifted towards lower temperatures with perovskite addition. At 353, 334, and 324 °C for PLA, PLA-Pero1, and PLA-Pero2 printed samples, respectively, which indicated a decrease in thermal stability of PLA polymer with the addition of perovskite crystals with a higher degree of crystallization.

Table 1 Summary of DSC heating curve of 3D-printed PLA and PLA-perovskite composites

Samples	T_g	T_c	T_m	ΔH_c (J g^{-1})	ΔH_m (J g^{-1})	X_c (%)
PLA	62.16	110.41	149.33	23.73	23.83	0.10
PLA-Pero1	66.02	118.84	151.51	24.65	25.26	0.62
PLA-Pero2	61.57	120.13	151.47	22.72	24.33	1.63

3.4. Optical properties

The photoluminescence behavior of the PLA/perovskite composites reveals sophisticated excitation-dependent emission mechanisms that demonstrate successful energy transfer processes within the hybrid materials (Fig. 4). The absorption characteristics (Fig. 4a) show that pristine PLA exhibits a distinct peak at 340 nm, while perovskite-embedded films display a red-shifted absorption at 375 nm, corresponding to $6s^2/6s^1p^1$ electronic transitions within the $[BiCl_6]^{3-}$ octahedral structure.[48] Under 400 nm excitation (Fig. 4b), the pristine PLA film exhibits strong blue fluorescence at 420 nm with a quantum yield of 20%, which might be attributed to π–π* transitions within degradation products formed on the PLA surface upon UV exposure, including carbonic acid, formic acid, acetic acid, and methyl acetate.[53] However, when excited at 350 nm (Fig. 4c), a dramatic shift occurs where PLA emission becomes severely quenched (PLQY drops to 2%) while the perovskite-containing films exhibit intense orange fluorescence centered at 610 nm. This wavelength-dependent behavior suggests that the UV-induced decomposition products on the PLA surface, which contribute to the blue fluorescence at 420 nm, are substantially less active at 350 nm excitation, coinciding with the emergence of efficient energy transfer to the embedded perovskite microcrystals, with the 610 nm emission corresponding to radiative recombination within the perovskite structures. The remarkable difference in photoluminescence quantum yield between PLA-Pero1 (2%) and PLA-Pero2 (47%) under 350 nm excitation demonstrates the critical importance of perovskite composition optimization. The wavelength-dependent PLQY studies (Fig. 4d–f) reveal that the 22-fold enhancement achieved by PLA-Pero2 is attributed to the Mn/Cd mixed cation system, which suppresses non-radiative decay pathways and creates optimal excitation conditions in the 300–350 nm range.[48] The PLA film shows increasing PLQY from 0.5% to 20% as excitation wavelength increases from 300 nm to 400 nm, suggesting multiple emission pathways with different

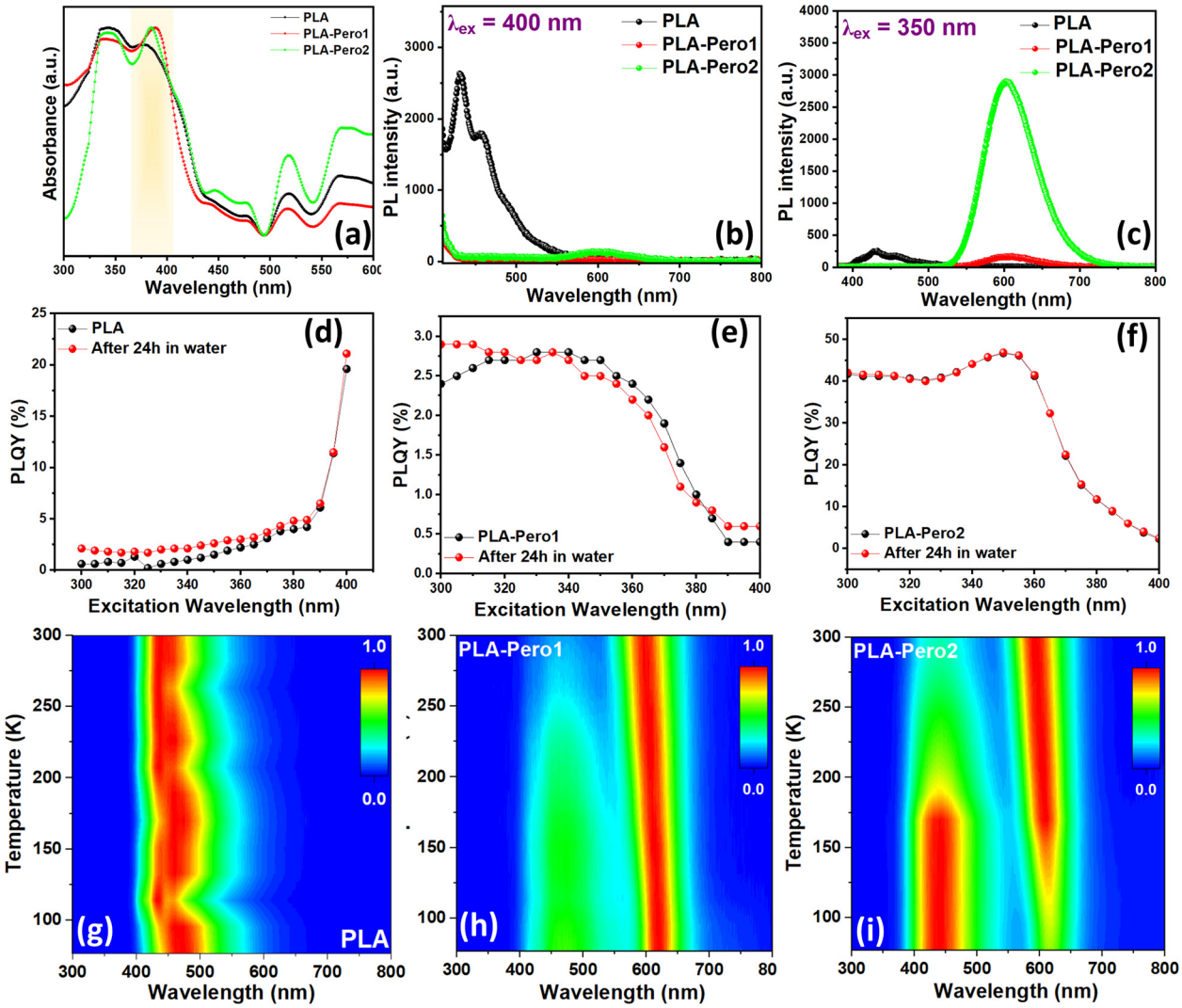

Fig. 4 Optical characterization of PLA, PLA-Pero1, and PLA-Pero2: (a) UV-Vis absorption spectra. (b) and (c) Photoluminescence (PL) spectra at 400 nm and 350 nm excitation wavelengths, respectively. (d)–(f) Photoluminescence quantum yield (PLQY) measurements at excitation wavelength range (300–400) nm. (g)–(i) Temperature-dependent PL mapping within temperature range (50–300 K).

efficiencies and wavelength-dependent competition between radiative and non-radiative processes. In contrast, the perovskite composites show optimal performance in the 300–350 nm range with a significant decline beyond 350 nm, indicating resonant excitation effects where maximum efficiency occurs when the excitation wavelength matches the perovskite absorption characteristics. The measured PL excitation (PLE) spectra show that the PL emissions of the PLA sample stem from its absorption peaks at 300 and 410 nm (Fig. S5). In contrast, both perovskite composites show a broad excitation band (Table S3) with peaks consistent with PLE profiles of perovskite powders, directly matching the absorption characteristics of the $[BiCl_6]^{3-}$ octahedral structures, as discussed previously.[48] Temperature-dependent studies (Fig. 4g–i) further reveal that both composites maintain stable emission characteristics with blue-shifting behavior from 610–650 nm upon heating, indicating thermal expansion effects on the crystal lattice that alter the band gap. The enhanced emission at lower temperatures suggests reduced thermal quenching of radiative recombination, with pronounced effects observed below 250 K for Pero1 and 170 K for Pero2. The matrix-perovskite interactions modify the electronic properties compared to pristine perovskite powders, demonstrating that the PLA matrix actively participates in the optical properties through energy transfer mechanisms rather than serving merely as passive support. The trace of this energy transfer process can also be observed in the room-temperature time-resolved photoluminescence (TRPL) spectrum (Fig. S6 and Table S4). Under 350 nm excitation, the average lifetime was found to be 3.8 μs and 151.7 μs for PLA-Pero1 and PLA-Pero2, respectively. The longer lifetime of PLA-Pero2 demonstrates that the Mn/Cd mixed cation system effectively suppresses non-radiative decay pathways while maintaining efficient radiative recombination, which is consistent with the high PLQY of PLA-Pero2 compared to

PLA-Pero1.[43,54] This comprehensive study of photoluminescence behavior confirms the creation of a synergistic hybrid system, where the polymer provides structural support and processability, while the perovskite components provide high-efficiency emission centers, resulting in optimized emission efficiency through controlled composition and excitation conditions.

3.5. X-ray scintillation properties

We investigate the scintillation properties of PLA/perovskite composites, focusing on attributes such as radioluminescence (RL), linearity, stability, and imaging capabilities using hard X-rays at the Advanced Photon Source (APS). When X-ray photons interact with the perovskite microcrystals embedded in PLA, they are converted into low-energy visible photons through the perovskite material. We measured the RL intensities under various X-ray fluxes, ranging from 7 × 1011 to 385 × 1011 photons per second. Both PLA/perovskite composites displayed RL spectra with peaks centered at 605 nm under X-ray excitation, representing a 5 nm blue shift from the PL emission at 610 nm, consistent with previously reported scintillator behavior.[55] As illustrated in Fig. S7a and b, a significant quenching of the RL intensity is observed when the X-ray flux decreases from 3.8 × 1013 photons per s to 7.11 × 1011 photons per s. This quenching occurs due to a reduction in the ionizing radiation energy deposited in the PLA/perovskite scintillators. To compare the RL spectra of both samples at different X-ray fluxes, we created a color mapping graph. As shown in Fig. 5a and b, the PLA/Pero2 film exhibits an RL intensity that is ten times stronger than that of the PLA/Pero1 film, which aligns with their corresponding PLQYs. Additionally, the RL intensities of both scintillators exhibit a strong

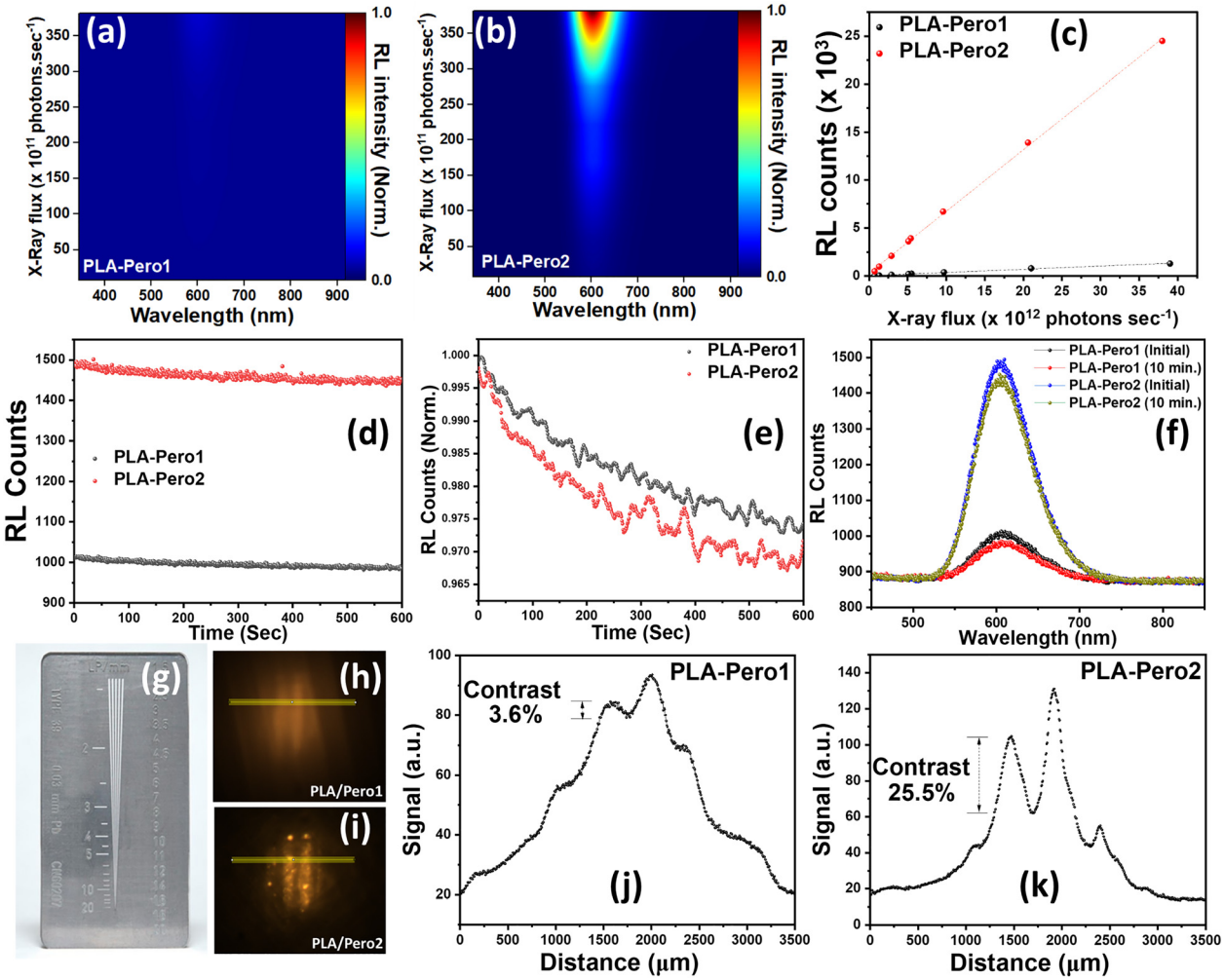

Fig. 5 Radioluminescence (RL) properties of PLA/perovskite composites. (a) and (b) Mapping of X-ray flux-dependent RL spectra of PLA/Pero1 and PLA/Pero2 samples, respectively. Linearity measurement: (c) X-ray flux-dependence of total radioluminescence signal of both samples. Stability measurement: (d) time-dependent RL decays from PLA/perovskite samples under continuous exposure to synchrotron X-rays with an average photon flux of 7.11 × 10^{11} photons per second. (e) Normalized RL decays. (f) Comparison between RL spectra of both samples at initial and after 10 minutes X-ray exposure. High-resolution X-ray imaging with PLA/perovskite composite films: (g) commercial resolution test Pb-stripe chart used for imaging with varying resolution targets from 2.0 to 20.0 LP mm^{-1} (line pair per mm) (h) and (i) X-ray images of 5 LP mm^{-1} target with the PLA/Pero1 and PLA/Pero2 scintillators where the yellow region in the inset is plotted as a line profile (j) and (k).

linear response to the incoming X-ray flux, as illustrated in Fig. 5c. The excellent linearity across multiple orders of magnitude demonstrates the robust charge carrier dynamics within the perovskite structure and suggests minimal saturation effects under the tested flux conditions. The superior detection sensitivity makes PLA/Pero2 favorable for high-dose imaging applications. Stability is a crucial characteristic of X-ray scintillators. The RL intensity of the PLA/perovskite films was measured over a continuous exposure period of 600 seconds to a substantially large X-ray photon flux of 7.11×10^{11} photons per second over an area of 900 μm by 700 μm. This photon flux is thousands of times greater than the typical limits encountered by medical scintillators.[56] Throughout exposure over 600 seconds, the RL intensity of the PLA/perovskite films demonstrated excellent stability, showing only a slight decrease in intensity, as illustrated in Fig. 5d. Specifically, the RL intensity of the PLA/Per1 and PLA/Pero2 films decreased by approximately 2.5% and 3.0%, respectively, compared to their initial intensity during the same exposure period, as shown in Fig. 5e and f. Next, we quantitatively analyze the spatial contrast of the PLA/perovskite scintillator films by imaging a commercial resolution test target (type 39, Supertech X-ray, Fig. 5g).[57] It is worth noting that the 600-second stability test is shorter than optimal for commercial applications, whereas it represents an initial assessment under extremely high flux conditions, *i.e.*, thousands of times higher than those typical of medical imaging. The PLA/Pero2 film (Fig. 5h) demonstrated higher resolution compared to the PLA/Pero1 film (Fig. 5i), successfully resolving a target of 5 line pairs per millimeter (LP mm^{-1}). The contrast ratios $\left(\frac{I_{max} - I_{min}}{I_{max} + I_{min}}\right)$ for the PLA/Pero2 and PLA/Pero1 films were 0.255 and 0.036, respectively, as illustrated in Fig. 5j and k. It is worth noting that the pristine PLA film was unable to detect the target, as depicted in Fig. S7c. This confirms that the X-ray scintillation occurs due to the presence of perovskite microcrystals embedded within the polymer matrix.

4. Conclusion

In summary, we addressed the fundamental trade-off between stability, optimal performance, and sustainability by developing 3D-printable PLA/perovskite composite films that embedded $Cs_4MnBi_2Cl_{12}$ and $Cs_4Cd_{0.68}Mn_{0.32}Bi_2Cl_{12}$ microcrystals within a biodegradable PLA polymer matrix. The water instability of halide perovskites was resolved while maintaining exceptional optical properties, with PLA-Pero2 achieving 47% PLQY, superior scintillation performance (605 nm emission, $<3\%$ degradation under high-flux X-rays), and imaging resolution of 5 LP mm^{-1}.

Author contributions

Amr Elattar: writing – review & editing, writing – original draft, methodology, investigation, data curation, and conceptualization. Abdullah Al Noman: investigation, formal analysis. Akil Dyson: investigation and formal analysis. J. S. Raaj Vellore Winfred: investigation, formal analysis, and review & editing. Burak Guzelturk: investigation, formal analysis, and review & editing. Logan T. Kearney: investigation, formal analysis, and review & editing. Adrienn Maria Szucs: investigation, formal analysis. Tarik Dickens: review & editing, funding acquisition, and conceptualization.

Conflicts of interest

There are no conflicts to declare.

Data availability

The data supporting this article have been included as part of the supplementary information (SI). Supplementary information is available. See DOI: **https://doi.org/10.1039/d5qm00667h**.

Acknowledgements

A. E., A. A., A. D. and T. D. acknowledge the NNSA MSIPP I-AM EMPOWER'D (Grant No. DE-NA0004004) at the FAMU-FSU College of Engineering. A. E., A. A., A. D. and T. D. acknowledge access to the CT scan facility at the Characterization Lab & *In situ* Facilities (CLIFF) at CePaST, Florida A&M University, which was financially supported by the National Science Foundation (MRI-1726035), the Department of Defense (W911NF2210148), and FAMU Vice President of Research. MicroXRF work performed at the Center for Rare Earths, Critical Minerals, and Industrial Byproducts at the National High Magnetic Field Laboratory, supported by the State of Florida through Contract # 0000071627. The National High Magnetic Field Laboratory is supported by the National Science Foundation under Grants DMR-1644779 and DMR-2128556, as well as by the State of Florida. A. M. S. acknowledges funding from the National Science Foundation under Grant No. DMR-2219906. X-Ray scintillation work performed at the Advanced Photon Source, U.S. Department of Energy Office (DOE) of Science User Facility, was supported by the U.S. DOE, Office of Basic Energy Sciences, under Contract No. DE-AC02-06CH11357. R. V. W. acknowledges the NSF MRI program (Grant No. CHE-1531629) for acquiring Edinburgh Instruments LP980-KS transient absorption system.

References

1 D. He, P. Chen, J. A. Steele, Z. Wang, H. Xu and M. Zhang, *et al.*, Homogeneous 2D/3D heterostructured tin halide perovskite photovoltaics, *Nat. Nanotechnol.*, 2025, **20**, 779–786.
2 Y. Lin, Z. Lin, S. Lv, Y. Shui, W. Zhu and Z. Zhang, *et al.*, A Nd@C82–polymer interface for efficient and stable perovskite solar cells, *Nature*, 2025, **642**, 78–84.
3 Y. Hong, S. Choi, J. Park, J. M. Kim, E. Kim and S. Lee, *et al.*, Metal halide perovskite photodetectors with hierarchical

hybrid Architectures: Interface Design for stability and optoelectric property enhancement, *Chem. Eng. J.*, 2025, **507**, 160584.

4 G. Hu, J. Guo, J. Jiang, L. Wang, J. Zhang and H. Chen, *et al.*, Capillary condensation-driven growth of perovskite nanowire arrays for multi-functional photodetector, *Light: Sci. Appl.*, 2025, **14**, 61.

5 A. Elattar, O. Okoli and T. Dickens, Optimization of $CsPbBr_3$/PVDF composite for enhanced UV photodetection application, *RSC Adv.*, 2024, **14**, 36416–36422.

6 S. Chi, Y. Chen, X. Li, J. Wang, Z. Zhao and Z. Li, *et al.*, Functional molecule surface infiltration treatment for efficient all-inorganic perovskite light-emitting diodes, *Chem. Eng. J.*, 2025, **514**, 162787.

7 Y. Lian, Y. Wang, Y. Yuan, Z. Ren, W. Tang and Z. Liu, *et al.*, Downscaling micro- and nano-perovskite LEDs, *Nature*, 2025, **640**, 62–68.

8 B. Wang, X. Yang, S. Chen, S. Lu, S. Zhao and Q. Qian, *et al.*, Flexible perovskite scintillators and detectors for X-ray detection, *iScience*, 2022, **25**, 105593.

9 A. Wibowo, M. A. K. Sheikh, L. J. Diguna, M. B. Ananda, M. A. Marsudi and A. Arramel, *et al.*, Development and challenges in perovskite scintillators for high-resolution imaging and timing applications, *Commun. Mater.*, 2023, **4**, 21.

10 M. D. Birowosuto, D. Cortecchia, W. Drozdowski, K. Brylew, W. Lachmanski and A. Bruno, *et al.*, X-ray Scintillation in Lead Halide Perovskite Crystals, *Sci. Rep.*, 2016, **6**, 37254.

11 Y. Yuan, G. Yan, R. Hong, Z. Liang and T. Kirchartz, Quantifying Efficiency Limitations in All-Inorganic Halide Perovskite Solar Cells, *Adv. Mater.*, 2022, **34**, 2108132.

12 C. Chen, T. Xuan, W. Bai, T. Zhou, F. Huang and A. Xie, *et al.*, Highly stable $CsPbI_3$:Sr^{2+} nanocrystals with near-unity quantum yield enabling perovskite light-emitting diodes with an external quantum efficiency of 17.1%, *Nano Energy*, 2021, **85**, 106033.

13 Y. Wang, N. Ding, D. Zhou, W. Xu, R. Sun and W. Li, *et al.*, ZnS-coated Yb^{3+} -doped perovskite quantum dots: A stable and efficient quantum cutting photon energy converter for silicon-based electronics, *Chem. Eng. J.*, 2024, **487**, 150347.

14 M. R. Filip, G. E. Eperon, H. J. Snaith and F. Giustino, Steric engineering of metal-halide perovskites with tunable optical band gaps, *Nat. Commun.*, 2014, **5**, 5757.

15 A. Elattar, H. Suzuki, R. Mishima, K. Nakao, H. Ota and T. Nishikawa, *et al.*, Single crystal of two-dimensional mixed-halide copper-based perovskites with reversible thermochromism, *J. Mater. Chem. C*, 2021, **9**, 3264–3270.

16 S. Jayaprakash Saiji, Y. Tang, S.-T. Wu, L. Stand, Y. Tratsiak and Y. Dong, Metal halide perovskite polymer composites for indirect X-ray detection, *Nanoscale*, 2024, **16**, 17654–17682.

17 A. Wibowo, M. A. K. Sheikh, L. J. Diguna, M. B. Ananda, M. A. Marsudi and A. Arramel, *et al.*, Development and challenges in perovskite scintillators for high-resolution imaging and timing applications, *Commun. Mater.*, 2023, **4**, 21.

18 B. Chen, S. Wang, Y. Song, C. Li and F. Hao, A critical review on the moisture stability of halide perovskite films and solar cells, *Chem. Eng. J.*, 2022, **430**, 132701.

19 K. Sun and P. Müller-Buschbaum, Shedding Light on the Moisture Stability of Halide Perovskite Thin Films, *Energy Technol.*, 2023, **11**, 2201475.

20 B. P. Kore, M. Jamshidi and J. M. Gardner, The impact of moisture on the stability and degradation of perovskites in solar cells, *Mater. Adv.*, 2024, **5**, 2200–2217.

21 B. Brunetti, C. Cavallo, A. Ciccioli, G. Gigli and A. Latini, On the Thermal and Thermodynamic (In)Stability of Methylammonium Lead Halide Perovskites, *Sci. Rep.*, 2016, **6**, 31896.

22 D. Han, K. Yang, C. Bai, F. Chen, Z. Sun and Y. Wang, *et al.*, Thermal and chemical durability of metal halide perovskite CsPbBr3 single crystals, *Chem. Eng. J.*, 2023, **475**, 146209.

23 A. Khorasani, F. Mohamadkhani, M. Marandi, H. Luo and M. Abdi-Jalebi, Opportunities, Challenges, and Strategies for Scalable Deposition of Metal Halide Perovskite Solar Cells and Modules, *Adv. Energy Sustainability Res.*, 2024, **5**, 2300275.

24 R. Li, L. Yao, J. Sun, Z. Sun, K. Zhang and J. Xue, *et al.*, Challenges and perspectives for the perovskite module research, *Chem*, 2025, 102542.

25 Q. Tu, D. Kim, M. Shyikh and M. G. Kanatzidis, Mechanics-coupled stability of metal-halide perovskites, *Matter*, 2021, **4**, 2765–2809.

26 F. Song, D. Zheng, J. Feng, J. Liu, T. Ye and Z. Li, *et al.*, Mechanical Durability and Flexibility in Perovskite Photovoltaics: Advancements and Applications, *Adv. Mater.*, 2024, **36**, 2312041.

27 M. Gandini, I. Villa, M. Beretta, C. Gotti, M. Imran and F. Carulli, *et al.*, Efficient, fast and reabsorption-free perovskite nanocrystal-based sensitized plastic scintillators, *Nat. Nanotechnol.*, 2020, **15**, 462–468.

28 B. Su, J. Jin, K. Han and Z. Xia, Ceramic Wafer Scintillation Screen by Utilizing Near-Unity Blue-Emitting Lead-Free Metal Halide $(C_8H_{20}N)_2Cu_2Br_4$, *Adv. Funct. Mater.*, 2023, **33**, 2210735.

29 L. Yang, H. Zhang, M. Zhou, L. Zhao, W. Chen and T. Wang, *et al.*, High-Stable X-ray Imaging from All-Inorganic Perovskite Nanocrystals under a High Dose Radiation, *J. Phys. Chem. Lett.*, 2020, **11**, 9203–9209.

30 L. Han, B. Sun, C. Guo, G. Peng, H. Chen and Z. Yang, *et al.*, Photophysics in Zero-Dimensional Potassium-Doped Cesium Copper Chloride $Cs_3Cu_2Cl_5$ Nanosheets and Its Application for High-Performance Flexible X-Ray Detection, *Adv. Opt. Mater.*, 2022, **10**, 2102453.

31 K. Děcká, F. Pagano, I. Frank, N. Kratochwil, E. Mihóková and E. Auffray, *et al.*, Timing performance of lead halide perovskite nanoscintillators embedded in a polystyrene matrix, *J. Mater. Chem. C*, 2022, **10**, 12836–12843.

32 A. Magi, M. Koshimizu, A. Sato, Y. Fujimoto, S. Kishimoto and T. Yanagida, *et al.*, Development of plastic scintillators loaded with perovskite quantum dots, *Jpn. J. Appl. Phys.*, 2022, **61**, SB1036.

33 J. Nie, C. Li, S. Zhou, J. Huang, X. Ouyang and Q. Xu, High Photoluminescence Quantum Yield Perovskite/Polymer Nanocomposites for High Contrast X-ray Imaging, *ACS Appl. Mater. Interfaces*, 2021, **13**, 54348–54353.

34 X. Wu, Z. Guo, S. Zhu, B. Zhang, S. Guo and X. Dong, *et al.*, Ultrathin, Transparent, and High Density Perovskite Scintillator Film for High Resolution X-Ray Microscopic Imaging. Advanced, *Science*, 2022, **9**, 2200831.

35 L. Lian, X. Wang, P. Zhang, J. Zhu, X. Zhang and J. Gao, *et al.*, Highly Luminescent Zero-Dimensional Organic Copper Halides for X-ray Scintillation, *J. Phys. Chem. Lett.*, 2021, **12**, 6919–6926.

36 H. Xu, W. Liang, Z. Zhang, C. Cao, W. Yang and H. Zeng, *et al.*, 2D Perovskite Mn^{2+}-Doped $Cs_2CdBr_2Cl_2$ Scintillator for Low-Dose High-Resolution X-ray Imaging, *Adv. Mater.*, 2023, **35**, 2300136.

37 N. Li, Z. Xu, Y. Xiao, Y. Liu, Z. Yang and S. Liu, Frank). Flexible, High Scintillation Yield $Cu_3Cu_2I_5$ Film Made of Ball-Milled Powder for High Spatial Resolution X-Ray Imaging, *Adv. Opt. Mater.*, 2022, **10**, 2102232.

38 R. E. Drumright, P. R. Gruber and D. E. Henton, Polylactic Acid Technology, *Adv. Mater.*, 2000, **12**, 1841–1846.

39 G.-X. Wang, D. Huang, J.-H. Ji, C. Völker and F. R. Wurm, Seawater-Degradable Polymers—Fighting the Marine Plastic Pollution, *Adv. Sci.*, 2021, **8**, 2001121.

40 M. Tabassum, Q. Zia, J. Li, M. T. Khawar, S. Aslam and L. Su, $FAPbBr_3$ Perovskite Nanocrystals Embedded in Poly(L–lactic acid) Nanofibrous Membranes for Enhanced Air and Water Stability, *Membranes*, 2023, **13**, 279–291.

41 Z. Yu, H. Li, X. Shan, S. Bao, S. Psulkowski and W. Guo, *et al.*, 3D Printed tandem X-Ray detector with halide perovskite-polymer composite semiconductor absorber, *Adv. Manuf.*, 2024, **1**(1), DOI: **10.55092/am20230002**.

42 X.-F. Qi, F. Zhang, Z.-P. Chen, X. Chen, M.-C. Jia and H.-F. Ji, *et al.*, Hydrothermal synthesis of stable lead-free $Cs_4MnBi_2Cl_{12}$ perovskite single crystals for efficient photocatalytic degradation of organic pollutants, *J. Mater. Chem. C*, 2023, **11**, 3715–3725.

43 J.-H. Wei, J.-F. Liao, X.-D. Wang, L. Zhou, Y. Jiang and D.-B. Kuang, All-Inorganic Lead-Free Heterometallic $Cs_4MnBi2Cl_{12}$ Perovskite Single Crystal with Highly Efficient Orange Emission, *Matter*, 2020, **3**, 892–903.

44 J. Li, J. Xiao, T. Lin, Z. Yan and X. Han, Lanthanide doping enabled multimodal luminescence in layered lead-free double perovskite $Cs_4MnBi_2Cl_{12}$, *J. Mater. Chem. C*, 2022, **10**, 7626–7632.

45 S. He, S. Fang, T. Han, T. Lang, M. Cai and H. You, *et al.*, Spectral Red Shift of $Cs_4Mn(Bi_{1-x}In_x)_2Cl_{12}$ Layered Double Perovskite by Adjusting the Microstructure of the $[MnCl_6]^{4-}$ Octahedron, *J. Phys. Chem. C*, 2021, **125**, 16938–16945.

46 N. P. Holzapfel, J. D. Majher, T. A. Strom, C. E. Moore and P. M. Woodward, $Cs_4Cd_{1-x}Mn_xBi_2Cl_{12}$—A Vacancy-Ordered Halide Perovskite Phosphor with High-Efficiency Orange-Red Emission, *Chem. Mater.*, 2020, **32**, 3510–3516.

47 X.-F. Qi, F. Zhang, Z.-P. Chen, X. Chen, M.-C. Jia and H.-F. Ji, *et al.*, Hydrothermal synthesis of stable lead-free $Cs_4MnBi_2Cl_{12}$ perovskite single crystals for efficient photocatalytic degradation of organic pollutants, *J. Mater. Chem. C*, 2023, **11**, 3715–3725.

48 N. P. Holzapfel, J. D. Majher, T. A. Strom, C. E. Moore and P. M. Woodward, $Cs_4Cd_{1-x}Mn_xBi_2Cl_{12}$—A Vacancy-Ordered Halide Perovskite Phosphor with High-Efficiency Orange-Red Emission, *Chem. Mater.*, 2020, **32**, 3510–3516.

49 H. A. L. Pham, V. H. Nguyen, T. Lee, V. C. Nguyen and T. D. Nguyen, Construction of BiOCl/bismuth-based halide perovskite heterojunctions derived from the metal-organic framework CAU-17 for effective photocatalytic degradation, *Chemosphere*, 2024, **357**, 142114.

50 K. Oksman, A. P. Mathew, D. Bondeson and I. Kvien, Manufacturing process of cellulose whiskers/polylactic acid nanocomposites, *Compos. Sci. Technol.*, 2006, **66**, 2776–2784.

51 X. Zhou, J. Deng, C. Fang, W. Lei, Y. Song and Z. Zhang, *et al.*, Additive manufacturing of CNTs/PLA composites and the correlation between microstructure and functional properties, *J. Mater. Sci. Technol.*, 2021, **60**, 27–34.

52 N. Najafi, M. C. Heuzey and P. J. Carreau, Polylactide (PLA)-clay nanocomposites prepared by melt compounding in the presence of a chain extender, *Compos. Sci. Technol.*, 2012, **72**, 608–615.

53 J. Zhou, S. Machida and K. Yamada, Enhanced UV-C resistance of 3D-printed poly(lactic acid)/glass fiber composites: Structural stability and sustainable design, *Next Mater.*, 2025, **9**, 101039.

54 Y. Huang, Y. Liu, Y. Liu, X. Tan, Y. Wang and Q. Xiao, *et al.*, Cobalt doping modulation of $Cs_4MnBi_2Cl_{12}$ double perovskite induces spin polarization for boosting photocatalytic reduction of CO_2, *Chem. Eng. J.*, 2025, **518**, 164734.

55 T. Jin, Z. Liu, J. Luo, J.-H. Yuan, H. Wang and Z. Xie, *et al.*, Self-wavelength shifting in two-dimensional perovskite for sensitive and fast gamma-ray detection, *Nat. Commun.*, 2023, **14**, 2808.

56 M. Gandini, I. Villa, M. Beretta, C. Gotti, M. Imran and F. Carulli, *et al.*, Efficient, fast and reabsorption-free perovskite nanocrystal-based sensitized plastic scintillators, *Nat. Nanotechnol.*, 2020, **15**, 462–468.

57 B. Guzelturk, B. T. Diroll, J. P. Cassidy, D. Harankahage, M. Hua and X.-M. Lin, *et al.*, Bright and durable scintillation from colloidal quantum shells, *Nat. Commun.*, 2024, **15**, 4274.